UNDERSTANDING SPACECRAFT FRAGMENTATION: SIMULATIONS AND EXPERIMENTS

Martin O. Steinhauser [1,2], Erkai Watson[1], Martin Schimmerohn[1]

[1] Fraunhofer-Institute for High-Speed Dynamics, Ernst-Mach-Institut, EMI, Eckerstrasse 4, 79104 Freiburg, Germany, Email: martin.steinhauser@emi.fraunhofer.de, erkai.watson@emi.fraunhofer.de, martin.schimmerohn@emi.fraunhofer.de

[2] University of Basel, Klingelbergstrasse 80, CH-4056 Basel, Switzerland, Email: martin.steinhauser@unibas.ch

ABSTRACT

We introduce a mesh-free computational model for simulation of hypervelocity impact (HVI) phenomena. Our proposed scheme is based on the Discrete Element Method (DEM) and this paper constitutes the first application of the DEM to the simulation of impact events in the hypervelocity regime [1]. We provide a quantitative computational analysis of impact generated debris clouds and a comprehensive parameter study by varying key parameters of our model. We compare our findings from the simulations with recent HVI experiments and outline the experimental methods that we develop to gain data on impact fragmentation for validating our approach. The ultimate objective of our work is to apply DEM for the simulation of complex spacecraft fragmentations resulting from space debris impact and spacecraft collisions.

1 INTRODUCTION

Since the beginning of the space age in the 20th century, the number of man-made debris particles in the Earth's orbit has constantly risen. Hence, there has been an ever-growing risk of active satellites being hit by space debris in the low earth orbit [2, 3, 4]. In order to assess the risk of future collision events, it is important to be able to predict the impact dynamics of the resulting debris cloud when space debris traveling at high velocity strikes a satellite structure.

The study of hypervelocity impact problems is of great interest for many engineering applications, such as spacecraft shield design [5]. The term hypervelocity generally refers to velocities so high that the strength of materials upon impact plays only a minor role and the material ceases to behave as a rigid solid, but more like a fluid [6]. Using the conservation of mass, momentum, and energy, one can make a simplified analysis by neglecting material strength, often referred to as a hydrodynamic model. The velocities at which materials start to behave like a fluid vary widely depending on the material's shock impedances and can be anywhere between 2-10 km/s [7]. For example, for aluminium, steel and quartz the hypervelocity phenomenon emerges with impact speeds of 5-6 km/s [8].

Numerical simulations of hypervelocity impact are needed when the size and velocity of the colliding objects are not easily accessible in ground experiments. Particularly, the characterization of spacecraft collisions with larger space debris objects in the relevant velocity regime would be a demanding task for experimental simulations. Nevertheless, the complex interaction of impact generated ejecta clouds strongly influences the generation and distribution of fragments in orbit. Semi-empirical models like the NASA break-up model are based on only a few model scale laboratory tests [9]. Sophisticated numerical simulations using hydrocodes are a perfect means to study complex break-up behaviour due to hypervelocity impact. For example, EMI's hydrocode SOPHIA [10] is currently used in an ESA funded study to simulate complex spacecraft fragmentations. SOPHIA applies finite element (FE) and smooth particle hydrodynamic (SPH) methods and, thus, is based on solving fundamental physical balance equation such as for linear momentum and energy according to continuum theory. Such simulations give important insight in the impact processes, but they are very complex in modelling and time-consuming in simulating. This limit their application for parametric investigations.

The development of DEM for spacecraft fragmentation simulation bears the potential of time-efficient parallel-izable simulation of complex phenomena. We started with stable, energy-conserving simulations of HVI scenarios that map the experimental setup where a sphere strikes a thin plate at hypervelocity. Our chosen interaction model works particularly well in the velocity range where the local stresses caused by impact shock waves markedly exceed the ultimate material strength.

The development of new computational methods for simulating fragmentation upon impact goes hand-in-hand with the advancement of experimental methods to investigate these failure cases in the laboratory. Experimental data is needed to validate the numerical models in generic test cases. As most of available fragmentation data relies on high-speed photographs, we also discuss our approach to apply laser-light sheet techniques and particle tracking methods to provide quantitative data for numerical method validation.

Proc. 7th European Conference on Space Debris, Darmstadt, Germany, 18–21 April 2017, published by the ESA Space Debris Office
Ed. T. Flohrer & F. Schmitz, (http://spacedebris2017.sdo.esoc.esa.int, June 2017)

2 SIMULATION MODEL

In our simulations, we aim at modelling the dynamics of impact failure and fracture behaviour of the material as observed in HVI experiments. For simplicity, we use mono--disperse spheres as basic discrete elements and adjust their interactions using attractive and repulsive potentials. It has been shown that the physical observables determined by such models for granular matter depend mainly on the interaction potentials and much less on the shape of the elements used for the discretization [11, 12].

A general principle used to develop our coarse-grained model is to begin with the simplest possible working model before adding more complexity. This simplifies the investigation of the complex interactions between material parameters. As we proceed to show, three parameters appear to be sufficient for reproducing the essential basic material properties that are important in a HVI setting where details of material strength can be simplified due to the overwhelmingly large shock pressures experienced in the case of HVI. The essential properties are, first, the resistance to pressure, second, the cohesive forces that keep the elements together to form a solid, and finally the microscopic failure.

2.1 Initial Setup

The particles are initiated into a regular cubic lattice structure, as seen in Fig.1. Each particle has two properties: mass m_i, and a length scale, diameter σ_i, according to the system's geometry. In the simulations presented here, we chose a mono--disperse configurations of particles, i.e., all masses $m_i = m$ and all lengths scales $\sigma_i = \sigma$ are the same for all particles. To form larger solids, many particles are connected with massless spring elements, also referred to as bonds. Then, a small random velocity taken from an equilibrium Boltzmann-distribution is applied to each particle. This random velocity ensures that the load transfer path is distributed through the material by disrupting the perfect alignments of the initial setup.

2.2 Particle Potentials

Newton's second law is used to evaluate the accelerations acting on each particle at every time step during the simulation and, thus, governs the dynamics of our model,

$$-\nabla_{ri}\Phi_{tot} = F_i = m\ddot{r}_i \qquad (1)$$

with Φ_{tot} being the interaction potential , i.e. the sum of all potentials acting on each particle i introduced in the next section. The accelerations can then be integrated to yield velocities and positions. The forces acting on each particle are defined via pair potentials. F_i comprises the force acting on the i-th particle due to the interaction potentials and m is the mass of one particle. Interactions

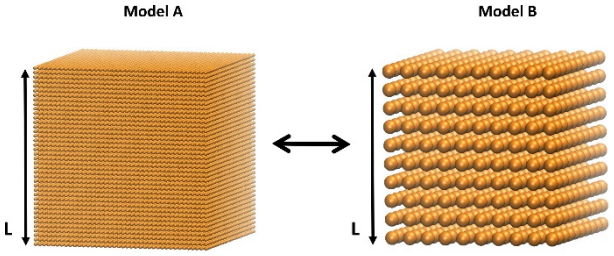

Figure 1. Particles are initiated into a regular cubic lattice. The model's properties are independent of number of particles.

can be classified as contact and bonded interactions. Bonded interactions correspond to the pairwise interactions of particles connected by a spring element. Contact interactions are experienced by particles whose centres are less than two radius lengths away from each other. We do not consider shear or tangential potentials in this basic model.

2.2.1 Contact Potentials

The Lennard–Jones potential

$$\phi_{rep}{}^{LJ}(r_{ij}) = \varepsilon\left\{\left(\frac{\sigma}{r_{ij}}\right)^{12} - \left(\frac{\sigma}{r_{ij}}\right)^{6}\right\} \qquad (2)$$

is a simple potential most commonly used in Molecular Dynamics simulations to model soft spheres [13, 14, 15], where σ is the diameter of each simulation particle, $r_{ij} = |r_j - r_i|$ is the distance between two particles, and ε is a pre–factor which has units of energy. The spheres are allowed to interpenetrate each other to a small extent (soft spheres), but quickly experience a strong repulsive potential according to $(\sigma/r_{ij})^{12}$. Beyond the particle diameter σ, there is a long range attractive component proportional to $(\sigma/r_{ij})^{6}$. The potential reaches a minimum at $r_{ij} = r_{min} = 2^{1/6}\sigma \approx 1.1225\sigma$, which defines the equilibrium distance r_{eq}.

In the presented model, the Lennard-Jones potential is modified slightly to refine the description of the physics of particle interactions: A cutoff distance, set to the potential minimum, is defined to remove the attractive component. Beyond this distance, the potential is defined to be zero. Shortening the potential's range also provides the benefit of reducing the computational time because each particle interacts with fewer neighboring particles which reduces the complexity of the interaction search algorithm. Additionally, the potential is shifted upwards by the factor ε to ensure smooth continuity with the spring potential such that:

$$\phi_{rep}(r_{ij}) = \begin{cases} \varepsilon\left[\left(\frac{\sigma}{r_{ij}}\right)^{12} - \left(\frac{\sigma}{r_{ij}}\right)^{6}\right] & \text{if } r_{ij} < r_{eq} \\ 0 & \text{otherwise} \end{cases} \qquad (3)$$

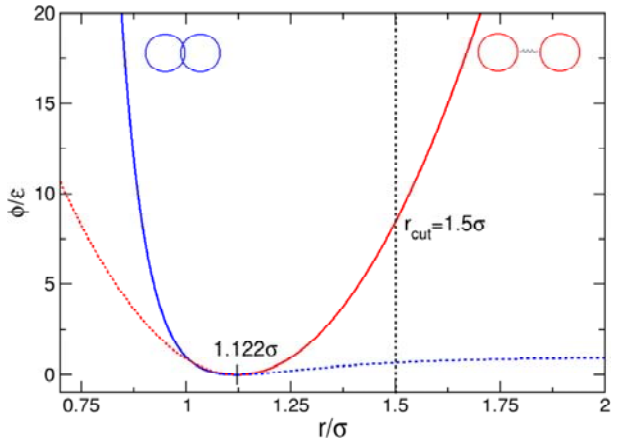

Figure 2. Repulsive (solid blue line) and cohesive (solid red line) potentials used in the model. The combined blue and red solid lines govern the forces acting on each particle pair; the dotted lines are excluded.

$$\phi_{rep}(r_{ij}) = \begin{cases} \varepsilon\left[\left(\frac{\sigma}{r_{ij}}\right)^{12} - \left(\frac{\sigma}{r_{ij}}\right)^{6}\right] & \text{if } r_{ij} < r_{eq} \\ 0 & \text{otherwise} \end{cases} \quad (3)$$

2.2.2 Bonded Potentials

Neighbouring particles are linked together to form a crystalline lattice structure. The bonded particle pairs can experience both cohesive and repulsive forces. A quadratic spring potential

$$\phi_{coh}(r_{ij}) = \begin{cases} 1/2\ \kappa(r_{ij} - r_{eq})^2 & \text{for } r_{ij} > r_{eq} \\ 0 & \text{otherwise} \end{cases} \quad (4)$$

is used for the cohesive component, and the potential of Eq.3 for the repulsive component. Parameter κ is in essence the spring constant and has units of energy divided by units of length squared. The equilibrium distance $r_{eq} = 2^{1/6}\sigma$ is set to coincide with the zero force distance of the potential $\phi_{rep}(r_{ij})$ of Eq.3. Fig.2 displays the various potential contributions to the total interaction potential for a particle pair. The modified Lennard--Jones potential is shown in blue, with the cut-off tail shown as a dotted line. Likewise, the quadratic potential is shown in red. The vertical dotted black line marks the distance at which the spring elements fail, r_{cut}. At $r_{ij} > r_{eq}$, the bonded particle pair experiences a cohesive force due to the spring potential. At $r_{ij} < r_{eq}$, the particles interaction is governed by the Lennard-Jones potential. At $r_{ij} = r_{eq}$ all forces are zero.

With the simplified model that we present in this paper, we deliberately exclude dissipation caused by friction or damping. However, some energy is removed from the system when failure of the material occurs. When the distance between two bonded particles exceeds a certain distance r_{cut}, the bond is considered to be broken and is

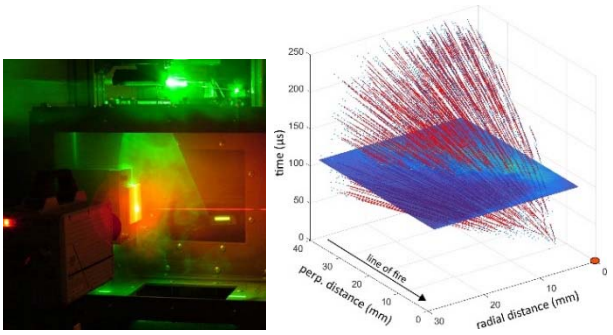

Figure 3. Individual particle tracking basing on selective illumination in experiment: Set-up and results.

removed. The two particles however, may continue to interact with each other or any other particle via the contact potential, and with other particles to which they may still be bonded.

With the three material parameters ε, κ, and r_{cut} we have developed a simple model with a minimal number of material parameters with the goal of exploring the potential of DEM for HVI simulations as a proof of principle. The essential parameters are ε representing resistance to pressure, κ representing cohesive forces, and r_{cut} representing microscopic failure.

3 EXPERIMENTS

Most of the data available for analysing fragmentation are high-speed photographs. Such photographs provide important information on the expansion behaviour of the resulting ejecta clouds, i.e. its dimension and propagation velocity. Cloud characteristics related to fragment size distribution and the evolving structure of the cloud provide a qualitative rather than quantitative analysis from optical high-speed visualization. However, quantitative information on hypervelocity fragmentation is needed to validate new numerical methods and applications. This is considered particularly important for DEM, as the interaction behaviour of the particles needs to be calibrated by appropriate test data.

We are currently developing experimental methods to identify individual ejecta particles and analyse their dynamic characteristics. The methods are based on selective illumination using laser light sheet techniques. The light sheet is aligned vertical to the target surface and in plane to the ejecta flow. The light scattered by the fragments is recorded with high-speed cameras. The high-speed images are than exploited by identifying single particles and track them on multiple frames. In experiments on geologic materials, we demonstrated spatio-temporal resolutions in the microsecond and micron range. Fig.3 shows an example of a set-up with visualized laser light sheet (green) and a results plot showing the detected particle occurrences and their trajectories.

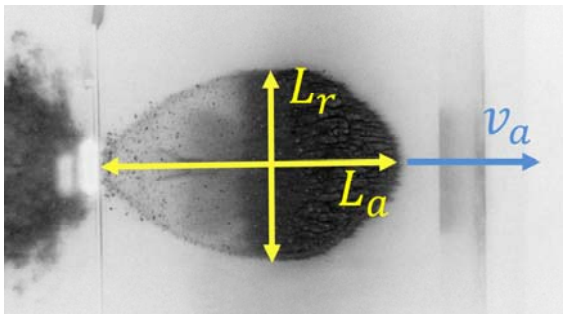

Figure 4. Experimental high-speed photograph of the debris cloud showing the cloud's length ratio $R = L_a/L_r$, and axial expansion velocity v_a.

We will optimize both the measurement method and the tracking algorithms in parallel to the development of the above presented DEM model as well as FE/SPH simulations in order to provide valuable experimental data for validation and calibration. For the first work on DEM in hypervelocity impact simulation presented in this paper, we confine ourselves to the comparison with high-speed photographs, as done in the next section.

4 RESULTS AND DISCUSSION

In this section, we discuss the results of our simulation study. After a detailed analysis of our choice of model parameters, we validate our simulations by comparison with experiments. This is followed by a comprehensive parameter study of HVI simulations, which we use to analyse the shape of the resulting debris cloud and the degree of material fragmentation after impact.

4.1 Choice of Model Parameters

The three free parameters of our model, ε, κ, and r_{cut}, are empirically fit by comparing the simulation results directly to a recent experiment involving aluminum spheres impacting aluminum plates. We used an experiment previously performed at our institute with an impact velocity $v_0 = 6.5$ km/s and a ratio of plate thickness to projectile length $t/D = 0.41$. Fig.4 shows a high-speed image of the experiment with the image's intensity inverted to allow for better viewing. Due to the challenges in performing HVI experiments, multiple experiments with the exact same parameters were unavailable. The experiment shown in Fig.4 was taken from a series of experiments studying the scalability of HVI, all of which had the same cloud expansion properties. This gives us some degree of confidence that the values measured from this single experiment are representative of HVI phenomena and therefore valid for fitting our model's parameters.

4.2 Validation with Experiment

We perform numerous HVI simulations at a variety of different impact velocities and t/D ratios and compare them to the corresponding experiments. One challenge

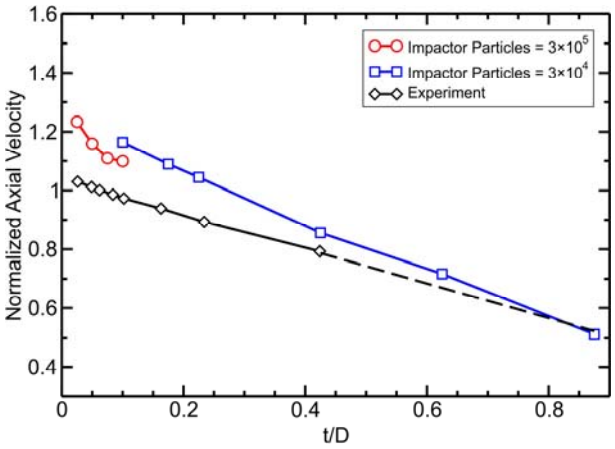

Figure 5. Debris cloud axial expansion velocity with $v_0 = 6.5$ km/s at different t/D ratios. The simulation results are compared to experiments [16].

is the limited quantifiable data, which can be obtained from HVI experiments. The extremely short time scale and limited instrumentation mean that often high-speed photographs are the only data available from the experiments. This restricts the quantitative comparison possible between our proposed numerical model and experiments. Nevertheless, a comparison is performed from the data that are available.

4.2.1 Extension of Debris Cloud

One of the measurable quantities from the experiments is the debris cloud's expansion velocity. Normalizing the expansion velocities with the impact velocity, v_a/v_0, allows us to meaningfully compare cloud characteristics even at different impact velocities.

In Fig.5, we compare the calculated debris cloud's axial expansion velocity with experimental values performed by Piekutowski [16] at an impact velocity of 6.7 km/s with varying t/D ratio. The diameter of the impacting sphere was 9.53 mm in the simulation and experiment. At larger t/D ratios, the simulation model had to be rescaled to avoid simulating an unreasonable number of particles as the plate thickness increased. The dotted line represents linearly extrapolated experimental data.

In Fig.5, the simulation over-predicts the expansion velocities, but still captures the overall decreasing trend. This decreasing trend is due to the increase in thickness of the target plate at higher t/D ratios. Since the sphere's size remains constant, a thicker plate requires more momentum to be transferred from the impactor particles to the plate particles. This increases the total mass in the debris cloud, but reduces its velocity.

The simulations' over-prediction of expansion velocities, as seen in Fig.5, result from the lack of a dissipative energy term in our model. Physically speaking, the passing of a shock wave is a highly transient process during which some of the kinetic

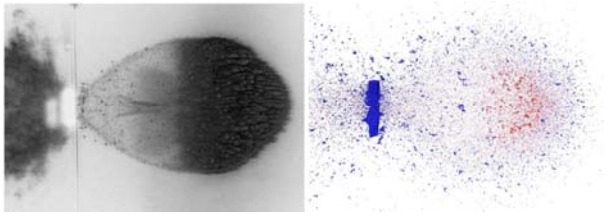

Figure 6. Simulations with high t/D ratios match the experiment closely with complete fragmentation of the impactor and a similar cloud shape. (left) High-speed photograph of experiment; (right) 3D simulation shown with $v_0 = 6.7$ km/s and $t/D = 0.425$.

energy is converted into heat as the material behind a shock wave experiences a sudden jump in thermodynamic variables such as pressure, energy, and density. This jump between two points of the Hugoniot curve takes place along the Rayleigh line and is a highly non-isentropic process. The rarefaction waves that bring the material back to ambient condition occur on an isentropic path. The difference in entropy gained in the process is therefore converted into heat, which is absorbed by the material. If the shock pressure is high enough, melting or vaporization will occur.

Without any dissipative effects in the model to account for heating and melting, all of the energy from the passing shock wave, except what is lost within the broken bonds, is recovered and transformed into kinetic and potential energy. This result in too much kinetic energy assigned to certain particles, leading to an overestimate of the cloud expansion velocity when compared to the experiment. A secondary effect of the lack of energy dissipation is a more diffuse boundary in the simulation debris cloud caused by a large variation in particle velocities. In contrast, the heating and melting in the experiment limit the particle velocities and help to create a sharper cloud boundary, as can be seen in Fig.6.

4.2.2 Shape and Degree of Fragmentation

Although the expansion velocities of the debris cloud provide useful and easily quantifiable information, they do not completely characterize the debris cloud; namely, the shape and degree of fragmentation of the cloud is not accounted for. Unfortunately, experiments do not generally provide a quantitative analysis of the fragmentation of the debris cloud distribution, so one usually depends on visual inspection. We provide such a visual comparison in Fig.6 and Fig.7, which show simulation and experimental snapshots of the debris clouds resulting from the impact of an aluminium sphere on plates of different thicknesses $v_0 \approx 6.7$ km/s. When the equivalent simulation and experiments are compared, it becomes apparent that the shape and degree of fragmentation play an important role in the debris cloud characterization.

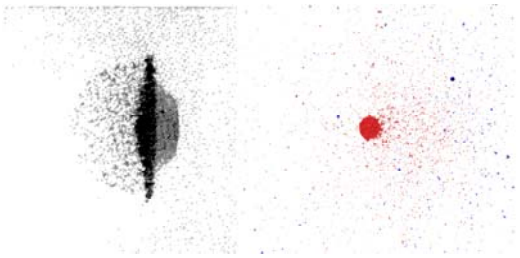

Figure 7. The shape of the debris cloud is highly affected by the t/D ratio. (left) High-speed radiograph of experiment [16]*; (right) 3D simulation shown with $v_0 = 6.7$ km/s and $t/D = 0.05$.*

Similarities in debris cloud shape and fragmentation level can be seen in Fig.6 showing impacts with high t/D ratios, but strong differences in shape and fragmentation occur at the low t/D ratio range. Fig.7 compares the experiment and simulation debris cloud resulting from an impact with $t/D = 0.05$, which exhibit very noticeable differences such as:

- The well defined front end (left side of cloud) as seen in the experiment is missing in the simulation.
- The large central fragment in the simulation did not fracture into a distinctive debris bubble behind the dense cloud center (right side of debris cloud) as seen in the experiment.

The lack of a well-defined front end structure is due to the absence of dissipative mechanisms in the model to account for heating and melting as previously explained. The failure to form a distinctive debris bubble at the rear of the cloud results from the model's limitation when the shock pressures are too low. The amplitude of a shock wave in HVI is dependent on the impact velocity and the combined geometry of target and impactor.

Upon impact, two shock waves form and propagate away from the interface between the plate and impacting sphere. When these shock wave reach the free back end of the plate or impacting sphere they are reflected as rarefaction waves, which are tensile waves. If the net tensile stress due to any rarefaction wave exceeds the fracture stress of the material, spallation will occur.

Because rarefaction waves propagate faster than shock waves, at small ratios of plate thickness to projectile length, i.e., the t/D ratio, the rarefaction wave reflected off the target plate may overtake and attenuate the shock wave in the projectile. Therefore, in HVI with a low t/D ratio, the impactor may only experience a weakened compressive wave. In such cases, the remaining amplitude of the compressive and tensile stresses in the impactor may no longer be many times higher than the material's shear and tensile strength. Our original assumption of material strength playing a very small role in the overall system behavior no longer holds true and the model ceases to yield accurate results.

5 CONCLUSIONS

In this paper, we explore the suitability of simulating impacts at velocities beyond 5 km/s with DEM. We propose a very simple model with three free parameters using two cohesive and repulsive potentials. In developing the model, we postulated that the extremely high pressures experienced by the material under HVI would relegate its material strength to a minor role. We assume that the material under impact behaves like a viscous fluid instead of a rigid solid, hence allowing a simplified model.

The model's parameters are determined by comparing the simulation results to experimental data taken from literature and performed at the Fraunhofer Ernst-Mach-Institute's hypervelocity testing facility. When evaluating the model's suitability, we find good correspondence between simulation and experiment when the impact conditions lead to strong shock waves propagating through the material, but poor results when the impact velocity or geometry hinders strong shocks from forming. We present here a comprehensive parameter study to evaluate the model's range of validity, in terms of impact velocity and geometry.

In a follow-up study currently underway, we are extending our model to account for dissipative effects such as heating and melting. We plan to investigate more complex and comprehensive models that will lead to accurate simulations at low shock pressures. We are also expanding the model to new impact geometries such as Whipple shields used for spacecraft shielding and to different impactor geometries such as cylinders. We plan to analyze the debris cloud resulting from such impacts with respect to fragment size, kinetic energy, cloud shape, and expansion velocity.

In parallel, we advance individual particle tracking methods in experiment to provide fragment characteristics and dynamics for validation and calibration of the numerical methods. The overall objective is to make a sophisticated approach available for the simulation of hypervelocity fragmentations of complex spacecraft.

ACKNOWLEDGEMENTS

We acknowledge financial support by the German Aeronautics and Space Research Center (DLR) under grant number 50LZ1502 “DEM-O”. Parts of this work have been published in [1].

REFERENCES

1. Watson, E, Steinhauser, M.O. (2017). Discrete Particle Method for Simulating Hypervelocity Impact Phenomena, *Materials* 10(4).
2. Wegener, P., Bendisch, J., Krag, H., Oswald, M., Stabroth, S., (2003). Population evolution in the GEO vicinity. *Adv. Space Res*. 34, 1171–1176.
3. Liou, J.C., Johnson, N.L., (2006). Planetary science. Risks in space from orbiting debris, *Science* 311, 340–341.
4. Liou, J.C., (2006). Collision activities in the future orbital debris environment, *Adv. Space Res*. 38, 2102–2106.
5. Liu, P., Liu, Y., Zhang, X. (2015). Improved shielding structure with double honeycomb cores for hypervelocity impact, *Mech. Res. Commun*. 69, 34–39.
6. Kinslow, R. (1970). *High-Velocity Impact Phenomena*, Academic Press: Cookeville, TN, USA.
7. Zukas, J.; Nicholas, T.; Swift, H. (1982). *Impact Dynamics*, John Wiley & Sons: New York, NY, USA.
8. Zhang, X.; Guanghui, J.; Huang, H. (2011). Fragment identification and statistics method of hypervelocity impact SPH simulation. *Chin. J. Aeronaut*. 24, 18-24.
9. Johnson, N.L. et al. (2001). NASA's new breakup model of EVOLVE 4.0. *Advances in Space Research* 28 (9), 1377-1384.
10. Ganzenmüller, G.C. (2015) An hourglass control algorithm for lagrangian smooth particle hydrodynamics. *Comp. Meth. Appl. Mech. Eng.* 286, 87-106.
11. Kadau, D., Bartels, G., Brendel, L., Wolf, D.E. (2002). Contact dynamics simulations of compacting cohesive granular systems. *Comp. Phys. Commun*. 147, 190–193.
12. Leszczynski, J.S. (2003). A discrete model of a twoparticle contact applied to cohesive granular materials. *Granul. Mat.* 5, 91–98.
13. Jones, J.E. (1924). On the determination of molecular fields. I. From the variation of the viscosity of a gas with temperature, *Proc. R. Soc. A Math. Phys. Eng. Sci*., 106, 441–462.
14. Steinhauser, M.O. (2013). *Computer Simulation in Physics and Engineering*, 1st ed.; deGruyter: Berlin, Germany, Boston, MA, USA.
15. Steinhauser, M.O. (2017) *Computational Multiscale Modeling of Fluids and Solids*, 2nd ed.; Springer: Berlin/Heidelberg, Germany.
16. Piekutowski, A.J. (1996). *Formation and Description of Debris Clouds Produced by Hypervelocity Impact*, Technical Report NASA Contractor Report 4707; University of Dayton Research Institute: Dayton, OH, USA.